This is an open access article published under an ACS AuthorChoice License, which permits copying and redistribution of the article or any adaptations for non-commercial purposes.

NANO LETTERS
Letter
pubs.acs.org/NanoLett

Atomic Scale Strain Relaxation in Axial Semiconductor III–V Nanowire Heterostructures

María de la Mata,[†] César Magén,[‡] Philippe Caroff,*[,§,∥] and Jordi Arbiol*[,†,⊥]

[†]Institut de Ciencia de Materials de Barcelona, ICMAB-CSIC, Campus de la UAB, 08193 Bellaterra, Catalonia, Spain

[‡]Laboratorio de Microscopías Avanzadas (LMA), Instituto de Nanociencia de Aragon (INA) -ARAID, and Departamento de Física de la Materia Condensada, Universidad de Zaragoza, 50018 Zaragoza, Spain

[§]Institut d'Électronique, de Microélectronique et de Nanotechnologie, UMR CNRS 8520, Avenue Poincaré, C.S. 60069, 59652 Villeneuve d'Ascq, France

[∥]Department of Electronic Materials Engineering, Research School of Physics and Engineering, The Australian National University, Canberra, Australian Capital Territory 0200, Australia

[⊥]Institució Catalana de Recerca i Estudis Avançats (ICREA), 08010 Barcelona, Catalonia, Spain

Supporting Information

ABSTRACT: Combination of mismatched materials in semiconductor nanowire heterostructures offers a freedom of bandstructure engineering that is impossible in standard planar epitaxy. Nevertheless, the presence of strain and structural defects directly control the optoelectronic properties of these nanomaterials. Understanding with atomic accuracy how mismatched heterostructures release or accommodate strain, therefore, is highly desirable. By using atomic resolution high angle annular dark field scanning transmission electron microscopy combined with geometrical phase analyses and computer simulations, we are able to establish the relaxation mechanisms (including both elastic and plastic deformations) to release the mismatch strain in axial nanowire heterostructures. Formation of misfit dislocations, diffusion of atomic species, polarity transfer, and induced structural transformations are studied with atomic resolution at the intermediate ternary interfaces. Two nanowire heterostructure systems with promising applications (InAs/InSb and GaAs/GaSb) have been selected as key examples.

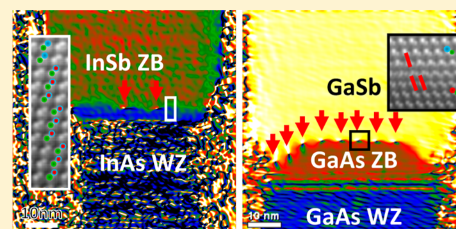

KEYWORDS: *Nanowire (NW), axial heterostructures, III–V, strain relaxation, atomic scale, Cs-corrected scanning transmission electron microscopy*

Due to their large aspect ratio, nanowires (NWs) are ideal candidates for the combination of highly mismatched materials preserving the crystal quality.[1,2] As a consequence of their morphology and free-standing nature, NWs can relieve the mismatch strain laterally over a short distance from the interface.[3−5] Moreover, unlike other systems, NWs offer the possibility of two different combination modes: radial (combining materials around the growth axis) and axial (combining the materials along the NW axis) to create the heterostructures.[6] The physical properties (e.g., electronic or optoelectronic) of the system will be influenced by the matching between the different combined materials: their relative orientation, the polarity at both sides of the interface or the presence of strain in the NWs.[7] It is widely known that strained materials show modified properties compared to the pristine bulk ones.[8] As elastic strain tunes the materials lattice constants, its presence in semiconductor heterostructures will change their electronic band alignments.[9−12] This paves alternative routes in bandgap engineering, through taking advantage of the bandgap modulation under uniaxial stress that allows the switching between different bandgap configurations.[13] Also playing with the strain in these materials, it is possible to enhance the carrier mobilities to get a better performance of the final devices,[8] or to create pseudoheterostructures by spatially confining the carriers within stressed material regions.[14,15] Nevertheless, strain could be released by the formation of misfit dislocations, which should be investigated to account for the plastic strain in these heterostructures. Not only the presence of strain in the materials but also the creation of misfit dislocations will influence the materials properties in different ways.[16] For instance, the creation of interfacial misfit dislocations negatively affect the performance of heterojunction tunnel diodes because they create acceptor states in the bandgap, contributing to the trap-assisted tunneling appearing when the device would be in the off-state.[17]

III−As/III−Sb heterostructure NWs are of special interest for their integration in advanced devices[18] as high speed electronics or long-wavelength optical devices,[19] as well as platform for the study of basic physical principles in condensed

Received: August 26, 2014
Revised: October 17, 2014
Published: October 20, 2014

 © 2014 American Chemical Society

matter such as Majorana fermions.[20,21] On one hand, III−Sb compounds show the narrowest bandgap, the highest electron/hole mobility (InSb/GaSb, respectively), the largest Landé g-factor[22] among binary semiconductor compounds, and a strong spin−orbit coupling. On the other hand, III−As compounds exhibit outstanding electron transport and optical properties, being used for high quality photonic devices (e.g., GaAs based single photon emitters,[23] room temperature lasers,[24,25] InAs based dual-band photodetectors or photovoltaic cells[26]). On the basis of the combination of these binary compounds, several authors have reported the feasibility of obtaining NW heterostructures by cation or anion switching. However, the growth of high quality crystal heterostructured NWs is challenging, especially for cation switching synthesis processes, using metal seed particles (mainly gold). Anion switching also has potential drawbacks: it is known that the high solubility of the group-V anions in the catalyst can result in kinking and graded interfaces[18] having detrimental implications for the later use of the synthesized structures. This is especially true for Sb, which is also a known surfactant, changing drastically the energy balance at interfaces.

In the present paper, we report a detailed study of axial III−As/III−Sb heterostructure NWs (III = In, Ga) through aberration-corrected high angle annular dark field (HAADF) scanning transmission electron microscopy (STEM). The HAADF technique is a *Z*-contrast imaging method[27−29] giving the exact atomic positions with chemical information, providing the requirements for a deep study of structural defects as dislocations.[30] The obtained data allows us to perform geometric phase analyses (GPA),[31] which is an accurate tool to account for strain within the NWs,[32] paying special attention to the interfaces and possible defect formation.[33] We compare the experimental atomic resolution images and strain maps with simulated models to fully understand the underlying mechanism governing the strain release. Interestingly, we found interfacial misfit dislocations as a mechanism to release the mismatch strain in both systems, which will be evaluated in detail. Although theoretical calculations predict the formation of misfit dislocations for the highly mismatched materials here presented (lattice constants and mismatches included in Tables 1 and 2),[34−36] most of the experimental results published neglect their presence.[37−43] Nevertheless, there are few papers evidencing misfit dislocations in heterostructured NWs (e.g., axial[18,44,45] or radial[46,47]), but a rigorous characterization at the atomic level is missing. In this paper, we show the InAs/InSb and GaAs/GaSb materials matching in a NW and the corresponding heterojunctions created through dislocated interfaces, addressed with atomic resolution. The possible formation of ternary compounds near the interfaces is also analyzed and compared with previous results. Finally, 3D atomic models for the strain relaxation mechanism are presented.

Table 1. Crystallographic Structures and Lattice Parameters of the Materials under Study

material	crystal structure	lattice parameters (Å)
InAs	zincblende	a = 6.0600
	wurtzite	a = 4.2851; c = 6.9975
GaAs	zincblende	a = 5.6535
	wurtzite	a = 3.9976; c = 6.5281
InSb	zincblende	a = 6.4800
GaSb	zincblende	a = 6.0959

InAs/InSb Synthesis. All nanowires have been grown by molecular beam epitaxy (MBE) using a thermally dewetted gold film as the source of the gold seed particles used to nucleate growth via a generic vapor phase epitaxy growth mechanism. The InAs/InSb nanowires were grown on an InP(111)B substrate by gas-source MBE following a procedure described in more detail previously.[48]

GaAs/GaSb Synthesis. The GaAs/GaSb nanowires were grown on a GaAs(111)B substrate by solid-source MBE. The stem was grown at 580 °C with a V/III ratio of 1.7, whereas the GaSb segment was grown at 450 °C with a V/III ratio of 22. The GaAs segment growth was terminated by switching the Ga flux off. Then, the sample was cooled down before switching the As_4 flux off while switching the Sb_2 flux on, prior to reopening the Ga flux. Both samples were cooled down to below 200 °C within a few minutes under vacuum conditions. More details of the growth processes can be found in the Supporting Information S1.

Transmission Electron Microscopy. The atomic resolution HAADF-STEM images have been acquired on a probe corrected FEI Titan 60−300 equipped with a high brightness field emission gun (XFEG) and a CETCOR corrector from CEOS to produce a probe size below 1 Å. The microscope was operated at 300 kV, with a convergence angle of 25 mrad and an inner collection angle of the detector of 58 mrad. Nanowires have been mechanically removed from the substrates and deposited on the STEM copper grid.[49]

3D Atomic Models and Image Simulations. All the 3D atomic models here presented have been created with the Rhodius software.[50,51] More details on the modeling geometry can be found at the Supporting Information S5. Once obtained the models, the image simulations have been carried out by using STEM CELL,[52,53] which is a free package software. We use a 300 keV electron beam with a convergence angle of 25 mrad, neglecting aberrations (defocus, astigmatism and higher order aberrations are set to 0). The collection angle goes from 60 to 200 mrad. Animated movies of the GaAs/GaSb and InAs/InSb nanowire heterostructures 3D Atomic Models generated for the present work can be found at: www.icmab.es/gaen/research/242

Geometric Phase Analysis. In order to map the deformation present at the NWs, we have used geometric

Table 2. Theoretical and Experimental Relative Mismatches Referred to the (−11−1) Plane of the Heterosystems Studied[a]

	(−11−1) mismatch		misfit spacing (Å)		
materials considered	calculated	experimental	calculated	experimental	planes between misfits
InAs(ZB)/InSb	6.5%		52		14−15/15−16
$InAs_{0.85}Sb_{0.15}$(ZB)/InSb	5.5%	≈ 5.5%	64	≈ 64	17/18
GaAs (ZB)/GaSb	7.8%	≈ 7.6%	46	≈ 48	13/14

[a]The first row is incomplete due to the lack of experimental data for the pure InAs/InSb interface.

dx.doi.org/10.1021/nl503273j | Nano Lett. 2014, 14, 6614−6620

phase analyses (GPA), developed by Hytch.[31] The GPA algorithm requires the selection of one or more Bragg reflection to be filtered and analyzed afterward. Here, we have employed a cosine type mask around the g = (−11−1) in both heterostructured systems. The radius of the mask has been optimized in the different analyses.

In the following, we present the atomic resolution study of the interface strain accommodation in two different III−As/III−Sb NW heterostructures. We start by analyzing the InAs/InSb heterointerface from the HAADF images and obtaining the strain maps. Before analyzing the images, the data has been treated through maximum entropy methods in order to account for the effective probe size.[30,54] After that, we create the 3D atomic models required to compare simulated and experimental data and discuss on the results. The second case presented is the GaAs/GaSb NW system, which we have analyzed by proceeding in the same way and compared to the previous one.

InAs/InSb. Axial InAs/InSb NW heterostructures are created from the former growth of InAs NWs as template stems for the further growth of InSb on their top. Notice that both phases involved in this system, InAs and InSb, have a theoretical relative mismatch of 6.5% (Table 2). The observed broadening of the NW diameter at the InSb (see Figure 1 a) has been attributed to a combination of compositional change in the droplet particle promoting its volume expansion due to uptake of In[41,55] together with an apparent diameter change due to the fact that the hexagons defining the cross section of the two segments of the NWs are rotated one with respect to the other by 30° around the growth direction. This latter rotation effect is linked to a different faceting, {1−100} for InAs and {110} for InSb, respectively.[56] However, the analyzed InAs/InSb sample in the present study preserves the faceting orientation of the InAs stem in the upper InSb section, being the InAs faceted by {1100} planes and the InSb by {110}, but in any case showing the same type of diameter broadening after the phase transition. Details on the NW morphology (intensity profiles across both InAs and InSb sections along with the surface plot display of one NW) and on the droplet−NW interface (showing the perfect structure matching of both phases, the $AuIn_2$ droplet and the InSb NW upper region) can be found in the Supporting Information S5.1 and S9. In the case of the InAs/InSb heterostructure, whereas InAs crystallizes in wurtzite (WZ) hexagonal structure[57] and grows along the [000−1] direction (As-polar), InSb shows zincblende (ZB) cubic structure[57] growing along the (1−11) plane, which is Sb-polar, as shown in Figure 1c, d (more details about the polarity assignment can be found at the Supporting Information S2.1). It means that the anionic polarity (As or Sb) is preserved across the interface. Although the phase transition from WZ to ZB occurs all at once through a perfectly flat interface (without any intermediate polytype or twinned phase), we observe that the first 3−4 nm of the ZB structure are 5.5% compressed. In Figure 1e, we show the dilatation map obtained by applying the GPA algorithm to the (1−1−1) InSb plane. After this region, going to the tip of the NW, the InSb lattice recovers its characteristic parameter and becomes completely relaxed. Paying attention to both, the GPA analyses and the atomic resolution HAADF images we see that the relaxation takes place partially through the formation of misfit dislocations to release the strain induced by the initial compressed ZB region (Figure 1e,f and Figure 2), as expected for radius above around 10 nm for this heterostructured system.[58]

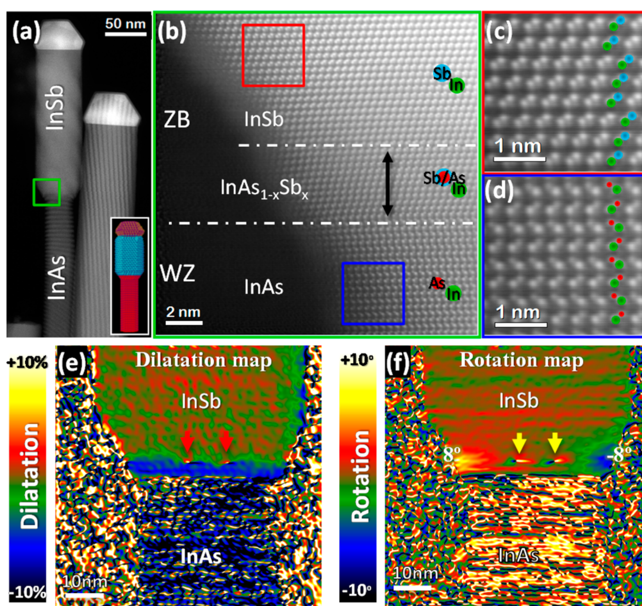

Figure 1. (a) Low magnification HAADF image of a couple of InAs/InSb NWs (the bright particle at the top is the droplet seed). Right bottom inset shows a 3D model of the whole system. An animated movie can be found at: www.icmab.es/gaen/research/242. (b) Atomic resolution image of the heterointerface, green square in (a). (c,d) Magnified detail of the InSb/InAs structure. In, As, and Sb positions are indicated by green, red, and cyan circles overlapping the atomic columns. (e) Dilatation map after applying GPA to the (−11−1) plane of the ZB region displayed in temperature color (scale codes included on the left side of the panel). Red arrows indicated the presence of misfit dislocations. (f) Rotation map of the (−11−1) ZB plane, showing symmetric rotation through the edges of the NW. Again, the arrows point the location of the misfit dislocations. More details are in the Supporting Information.

A careful inspection at the compressed region it is needed to understand the location of the misfit dislocations 3−4 nm apart from the phase transition. Thus, we take advantage of the Z dependence of the HAADF technique,[27−29] performed with atomic resolution,[59,60] allowing the atomic identification by simple intensity profile integration.[61−64] We have already mentioned that both, the InAs stem and the InSb upper section of the NW grow along anionic polar directions, meaning that the In is always below the cation in every dumbbell. Note that this implies an intensity reversal when comparing the two different dumbbell couples (In−As vs In−Sb), that is, the As intensity is dimmer than the In one for the InAs dumbbell ($Z_{In} > Z_{As}$, see Table 3), whereas the Sb is brighter than the In for the InSb dumbbell ($Z_{In} < Z_{Sb}$, see Table 3). Interestingly, we can clearly see that in the concerned compressed region the intensity inversion is progressive, evidencing an Sb gradient (more details can be found in the Supporting Information Figure S3).

EDX measurements reported in ref 41 detected the presence of an Sb gradient through the interface. However, due to the interface abruptness and the poor spatial resolution of the technique, the authors claimed that no Sb interdiffusion took place. Our atomic resolution experiments support the reliability of the previous EDX results, suggesting a clear Sb gradient along few nanometers after the phase transition. From these results, we can precisely observe that the sudden change from WZ to ZB phases takes place immediately after the introduction of Sb, resulting in a sharp interface (phase

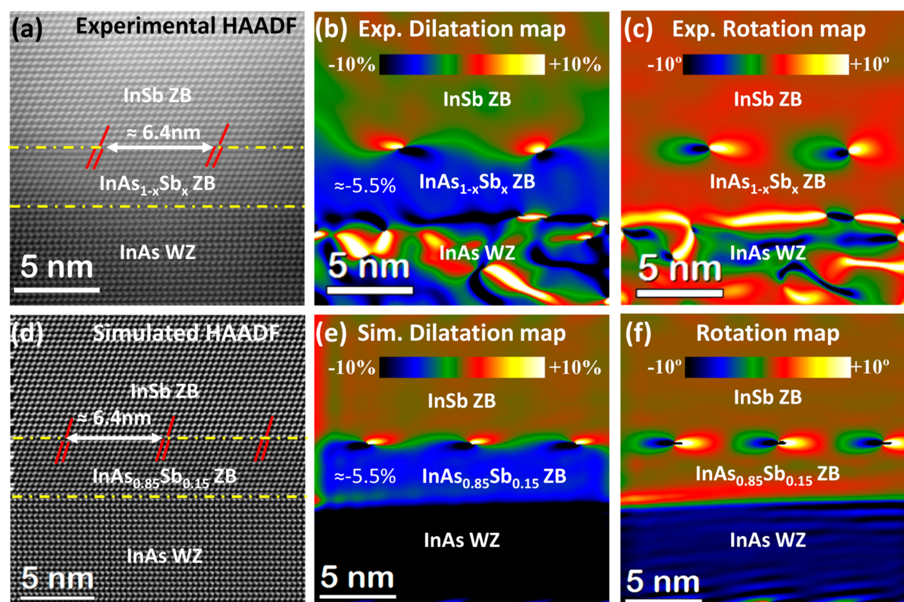

Figure 2. (a−c) Experimental data obtained at the InAs/InSb heterointerface. (a) Atomic resolution HAADF image showing two misfit dislocations. (b,c) GPA dilatation and rotation maps, respectively, for the (−11−1) plane. (d−f) Simulated images and maps calculated accounting for an intermediate $InAs_{0.85}Sb_{0.15}$ layer between the pure InAs WZ and the InSB ZB. (d) Simulated HAADF image. (e,f) Dilatation and rotation maps, respectively, obtained by applying GPA to the (−11−1) ZB plane. All the simulated HAADF images have been calculated by means of STEM CELL software[52] and the 3D models used for the calculations have been created by Rhodius.[50]

Table 3. Atomic Number, *Z*, of the Constituents Forming the Analyzed Structures

element	As	Ga	In	Sb
Z	33	31	49	51

transition interface). It is known that III−antimonides tend to crystallize in pristine ZB phase, even in the case of ternary compounds with small Sb quantities (i.e., $GaAs_{1-x}Sb_x$, $InAs_{1-x}Sb_x$).[48,65,66] Thus, as the right composition for the InSb growth is not reached yet (we have not consumed completely the As previously introduced in the seed particle), we initially obtain an $InAs_{1-x}Sb_x$ transition region, with smaller cell constant than the pure InSb. On the basis of the measured lattice parameter on the compressed region and assuming a Vegard's law behavior for the system, we have calculated the Sb content to be around 15% in that area (Supporting Information S2.1). Even though we could detect a slight radial InSb overgrowth around the last planes of the InAs stem (see Supporting Information Figure S7), as we focused on the lateral edges of the NW, the observed structure when viewing the center of the interface corresponds to the actual core of the NW (supported by image simulations performed). This means that the estimated Sb content is actually incorporated at the InAs crystalline structure, promoting the observed lattice parameter expansion. Similar observations have been reported in ref 43, where the authors found a compressed ZB region above the heterointerface in axial InAs/GaSb NWs due to the formation of $In_{0.5}Ga_{0.5}As$ at the interfacial region.

Modeling the system by taking into account the formation of an axial segment with $InAs_{0.85}Sb_{0.15}$ composition before the pure InSb section, we have obtained strain maps in good agreement with the experimental ones. The results of the simulations are displayed in Figure 2d−f. As already mentioned, the Sb incorporation promotes the sudden phase transition from WZ to ZB. From there, the Sb is gradually introduced into the structure and after 3−4 nm showing $InAs_{0.85}Sb_{0.15}$ mean composition, the system gets the right InSb stoichiometry (more simulated systems can be found in the Supporting Information Figure S4). The lattice mismatch between the $InAs_{0.85}Sb_{0.15}$ and InSb is around −5.5%, inducing the formation of misfit dislocations spaced 6.4 nm (see Figure 2 d and Table 2). In the central region of the interface, we can find the expected misfit dislocations. However, closer to the NW edges misfit dislocations do not show up (Figure 1e,f). Instead, we observed a symmetric plane rotation, in the attributed $InAs_{0.85}Sb_{0.15}$, reaching $\pm 8°$ (Figure 1 f) from the center of the NW to the edges (with opposite sign at both visible edges). This plane rotation releases strain elastically, being the rest of the NW relaxed. In this way, we atomically show that both relaxation mechanisms may coexist at the same interface: plastic deformation (misfit dislocations) at the central part of the NW and elastic deformation (plane bending) strain release near the edges.

It is worth mentioning that every analyzed NW (up to 8) show misfit dislocations appearing few nanometers away from the phase transition. The number of dislocations and the spacing between them are strongly dependent on the diameter of the heterostructure (see Supporting Information Figure S2) and the amount of Sb initially incorporated, but the strain release always occurs by a combination of plastic deformation at the center of the interface and elastic deformation at the edges.

GaAs/GaSb. Another example combining arsenide and antimonide compounds to create an anionic exchange interface is found in axial GaAs/GaSb NWs, with a theoretical mismatch of 7.8% (Table 2). As in the previous case, the growth starts by creating the arsenide stems (GaAs) for the later growth of the antimonide counterpart (GaSb) on their top. The GaAs stems have pure WZ structure, as usual, growing along the [000−1] direction (As-polar), whereas the GaSb grows with pristine ZB structure along the [1−1−1] direction, being also anionic polarized (Sb-polar). The phase transition from WZ to ZB

takes place before the chemical interface, meaning by this that the last GaAs nanometers already have ZB structure, being the (1−1−1) the growth plane. Details of the atomic arrangements for the three crystallographic phases involved (GaAs WZ, GaAs ZB, and GaSb ZB) are shown in Figure 3b−d, where the atomic constituents are identified. Further details can be found in the Supporting Information S2.2.

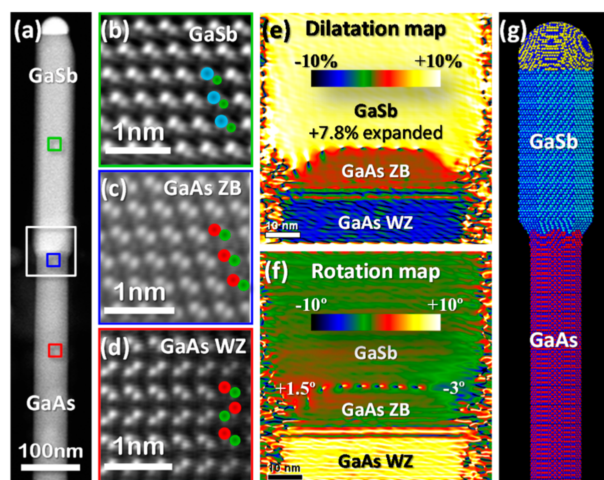

Figure 3. (a) Low magnification HAADF image of one analyzed GaAs/GaSb NW. (b−d) Atomic resolution images of the three different crystallographic phases contained in the NW. (e,f) Dilatation/rotation maps calculated by means of GPA on the (−11−1) plane. (g) 3D model of the GaAs/GaSb NW system, with core−shell like interface. An animated movie of the 3D atomic model can be found at: www.icmab.es/gaen/research/242.

Contrary to the InAs/InSb system where the interface between both materials was flat, in the present case, the interfaces are bended. Kanungo et al. described a similar curvature in the growth front.[44] However, in their work, the gold-free InAs stem was grown first inside a SiO_x tube, then was etched and annealed prior to a second growth giving rise to a convex surface prior to the growth of the III−Sb segment. The curved interface in our case could be the result of a drastic change on the gold-containing alloy seed wetting configuration: due to surface energy differences occurring during the switching sequence or a change of its volume, eventually the particle wets both sides of the GaAs stems, as inferred in other works.[67,68] Truncation of the growth plane along the contact line between the NW and the droplet has been observed in several semiconductor NWs,[69,70] allowing a deep characterization of the growth dynamics.[71] Wang et al.[71] found that the supersaturation of the droplets drove a fast 1D growth on the truncated facets (belonging to the {113} and {120} family planes) followed by a slower 2D growth on the main facets of the NW. Falub et al.[72] also reported the formation of {113} truncation planes while growing Ge NWs on Si and related their degree of development with the growth temperature. Our spectroscopic measurements (shown in Supporting Information, Figure S8), performed by means of electron energy loss spectroscopy (EELS), evidence the lateral (radial) growth of the GaSb around the last nanometers of the GaAs while growing the axial system. Notice the truncation of the GaAs growth front, which has been filled by the GaSb grown afterward. Thus, the interface of the NW can be considered as a core−shell interface (referred to its shape), where the core is formed by the GaAs (ZB) stem (bordered by {113} truncation planes) and the shell forms from the radial overgrowth of GaSb, explaining the interface morphology (see the 3D model included in Figure 3h and Supporting Information Figure S11).

When performing GPA in this system, we found the interface full of almost periodic misfit dislocations, spaced about 4.8 nm (averaged over 7 NWs) (see Figure 3e,f), perfectly visible in the atomic resolution HAADF images (Figure 4 a). For a matter of consistency, we have also created a 3D model of the NW (Figure 3g and Supporting Information Figure S4) to obtain the simulated images and strain maps, which are included in Figure 4d−f. Comparing the lattice parameters at both sides of the interface, we found that the GaSb material is 7.6% expanded

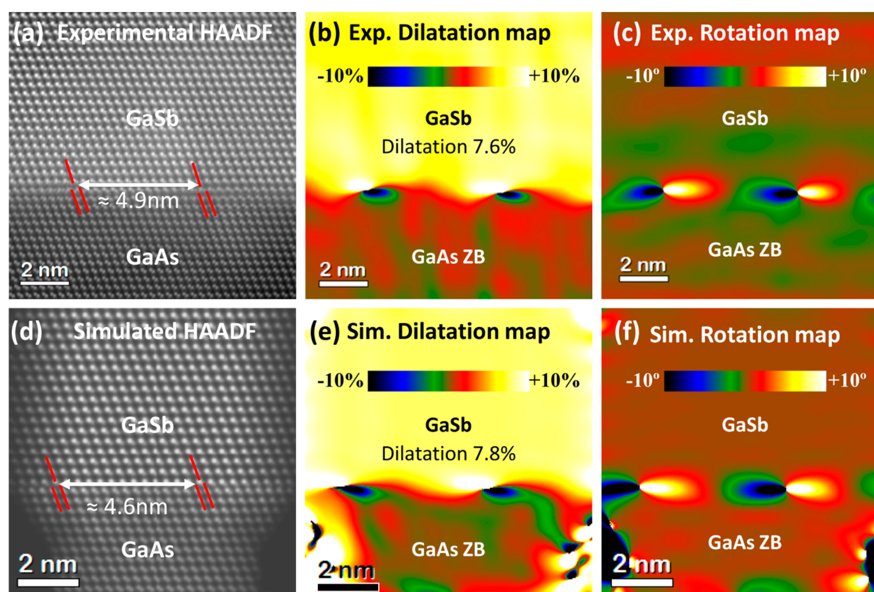

Figure 4. (a−c) Experimental data obtained at the GaAs/GaSb heterointerface. (a) HAADF image showing two misfit dislocations 4.9 nm apart. (b,c) Dilatation and rotation maps, respectively, obtained by performing GPA on the image in (a). (d−f) Simulated data on the GaAs/GaSb interface. (d) HAADF simulated image. (e,f) Simulated dilatation and rotation map, respectively, obtained by performing GPA on the image in (d).

dx.doi.org/10.1021/nl503273j | *Nano Lett.* 2014, 14, 6614−6620

in average compared to the GaAs ZB, in good agreement with theoretical calculations (see Table 2). Going one step further, it can be noted that the first 1.5 nm of the GaSb section are slightly compressed yet (lattice dilatation around 7%). This feature is pointed out by the dilatation discrepancies between the experimental and simulated strain maps near the heterointerface (Supporting Information Figure S4). However, this detail goes unnoticed by direct observation of the color maps and explains the small difference between the experimental and simulated dilatation near the interface (+7.6% and +7.8%, respectively). Thus, the relaxation of the GaSb lattice takes place through the formation of almost periodic misfit dislocations adapted to the convex shape of the interface, as in the case of the planar growth.[73,74] Regarding the elastic strain component, we detect a small plane rotation through the NW edges at the interfacial region where the NW is wider, as shown in the rotation map included in Figure 3d. Notice the absence of dislocations on the right side of the NW. There, the strain release occurs elastically by a 3° rotation of the analyzed planes. Contrary, on the left side of the NW the mismatch strain is almost fully released by the formation of dislocations, whereas the planes are bended only +1° in this region (combining both elastic and plastic (misfits) strain release).

Driven by the need of an atomic characterization of III−As/III−Sb axial interfaces integrated in NWs, we have depicted the strain release mechanisms for the InAs/InSb and GaAs/GaSb NW systems. We have found that in both heterostructures, the mismatch strain results in a combination of both plastic and elastic deformations. On one hand, in the InAs/InSb NW case, we have found an abrupt phase change from InAs WZ to InAs ZB, promoted by the introduction of Sb along 3−4 nm (Sb-gradient). This region is 5.5% compressed compared to the pure InSb section, which is compensated by the creation of misfit dislocations in the central area of the NW (plastic deformation) and by an 8° plane rotation through the edges (elastic deformation). After the interface, the NW is completely relaxed. On the other hand, the GaAs/GaSb system shows a core−shell interface due to GaSb overgrowth around the GaAs stem. Thus, the shape of the interface is curved and full of almost periodic dislocations, especially at the central part of the NW. Once again, at the edges of the NW the strain release occurs partially by the creation of misfits, contrary to what was stated in most of the previous works found in literature, and partially by plane bending. These results show with unprecedented resolution the different mechanisms that may combine for strain relaxation in a complex NW interface, allowing a fully epitaxial growth of the heterostructures. The 3D atomic models obtained can be extremely useful in order to compute and understand the final physical performance of the interfaces studied.

■ ASSOCIATED CONTENT

Ⓢ Supporting Information

Extended details on synthesis and experimental methods, expanded characterization, chemical analyses, 3D atomic models, and droplet−NW interface detailed study. This material is available free of charge via the Internet at http://pubs.acs.org.

■ AUTHOR INFORMATION

Corresponding Authors

*E-mail: philippe.caroff@anu.edu.au.

*E-mail: arbiol@icrea.cat.

Notes

The authors declare no competing financial interest.

■ ACKNOWLEDGMENTS

J.A. acknowledges the funding from the Spanish MINECO MAT2014-51480-ERC (e-ATOM), EU ERANet-RUS Project PRI-PIMERU 2011-1422, and Generalitat de Catalunya 2009SGR770 and 2014SGR1638. M.d.l.M. thanks CSIC Jae-Predoc program. P.C. would like to thank Xavier Wallart for scientific discussions, the French National Research Agency (ANR), TERADOT Project (ANR-11-JS04-002-01) and the Australian Research Council (ARC), Future Fellowship project (FT120100498), for financial support.

■ REFERENCES

(1) Robinson, R. D.; Sadtler, B.; Demchenko, D. O.; Erdonmez, C. K.; Wang, L. W.; Alivisatos, A. P. *Science* **2007**, *317*, 355−358.

(2) Gudiksen, M. S.; Lauhon, L. J.; Wang, J.; Smith, D. C.; Lieber, C. M. *Nature* **2002**, *415*, 617−620.

(3) Bjo1rk, M. T.; Ohlsson, B. J.; Sass, T.; Persson, A. I.; Thelander, C.; Magnusson, M. H.; Deppert, K.; Wallenberg, L. R.; Samuelson, L. *Nano Lett.* **2002**, *2*, 87−89.

(4) Larsson, M. W.; Wagner, J. B.; Wallin, M.; Håkansson, P.; Fröberg, L. E.; Samuelson, L.; Wallenberg, L. R. *Nanotechnology* **2007**, *18*, 015504.

(5) Dick, K. A.; Bolinsson, J.; Borg, B. M.; Johansson, J. *Nano Lett.* **2012**, *12*, 3200−3206.

(6) Li, Y.; Qian, F.; Xiang, J.; Lieber, C. M. *Mater. Today* **2006**, *9*, 18−27.

(7) Schuster, F.; Laumer, B.; Zamani, R. R.; Magén, C.; Morante, J. R.; Arbiol, J.; Stutzmann, M. *ACS Nano* **2014**, *8*, 4376−4384.

(8) Signorello, G.; Karg, S.; Björk, M. T.; Gotsmann, B.; Riel, H. *Nano Lett.* **2013**, *13*, 917−924.

(9) Hong, K.-H.; Kim, J.; Lee, S.-H.; Shin, J. K. *Nano Lett.* **2008**, *8*, 1335−1340.

(10) Ng, W. L.; Lourenço, M. A.; Gwilliam, R. M.; Ledain, S.; Shao, G.; Homewood, K. P. *Nature* **2001**, *410*, 192−194.

(11) Pryor, C. E.; Pistol, M.-E. *Phys. Rev. B* **2005**, *72*, 205311.

(12) Pryor, C. E.; Pistol, M.-E. *Phys. Rev. B* **2008**, *78*, 115319.

(13) Signorello, G.; Lörtscher, E.; Khomyakov, P. A.; Karg, S.; Dheeraj, D. L.; Gotsmann, B.; Weman, H.; Riel, H. *Nat. Commun.* **2014**, *5*, 3655.

(14) (a) Nam, D.; Sukhdeo, D. S.; Kang, J.-H.; Petykiewicz, J.; Lee, J. H.; Jung, W. S.; Vučković, J.; Brongersma, M. L.; Saraswat, K. C. *Nano Lett.* **2013**, *13*, 3118−3123.

(15) Pistol, M.-E.; Pryor, C. E. *Phys. Rev. B* **2009**, *80*, 035316.

(16) Queisser, H. J.; Haller, E. E. *Science* **1998**, *281*, 945−950.

(17) Bessire, C. D.; Bj€ork, M. T.; Schmid, H.; Schenk, A.; Reuter, K. B.; Riel, H. *Nano Lett.* **2011**, *11*, 4195−4199.

(18) Borg, B. M.; Dick, K. A.; Ganjipour, B.; Pistol, M.-E.; Wernersson, L.-E.; Thelander, C. *Nano Lett.* **2010**, *10*, 4080−4085.

(19) Thelander, C.; Agarwal, P.; Brongersma, S.; Eymery, J.; Feiner, L. F.; Forchel, A.; Scheffler, M.; Riess, W.; Ohlsson, B. J.; Gösele, U.; Samuelson, L. *Mater. Today* **2006**, *9*, 28−35.

(20) Mourik, V.; Zuo, K.; Frolov, S. M.; Plissard, S. R.; Bakkers, E. P. A. M.; Kouwenhoven, L. P. *Science* **2012**, *336*, 1003−1007.

(21) Deng, M. T.; Yu, C. L.; Huang, G. Y.; Larsson, M.; Caroff, P.; Xu, H. Q. *Nano Lett.* **2012**, *12*, 6414−6419.

(22) Nilsson, H. A.; Caroff, P.; Thelander, C.; Larsson, M.; Wagner, J. B.; Wernersson, L.-E.; Samuelson, L.; Xu, H. Q. *Nano Lett.* **2009**, *9*, 3151−3156.

(23) Heiss, M.; Fontana, Y.; Gustafsson, A.; Wüst, G.; Magen, C.; O'Regan, D. D.; Luo, J. W.; Ketterer, B.; Conesa-Boj, S.; Kuhlmann, A. V.; Houel, J.; Russo-Averchi, E.; Morante, J. R.; Cantoni, M.; Marzari, N.; Arbiol, J.; Zunger, A.; Warburton, R. J.; Fontcuberta i Morral, A. *Nat. Mater.* **2013**, *12*, 439−444.

(24) Saxena, D.; Mokkapati, S.; Parkinson, P.; Jiang, N.; Gao, Q.; Tan, H. H.; Jagadish, C. *Nat. Photonics* **2013**, *7*, 963−968.
(25) Mayer, B.; Rudolph, D.; Schnell, J.; Morkötter, S.; Winnerl, J.; Treu, J.; Müller, K.; Bracher, G.; Abstreiter, G.; Koblmüller, G.; Finley, J. J. *Nat. Commun.* **2013**, *4*, 2931.
(26) Wei, W.; Bao, X.-Y.; Soci, C.; Ding, Y.; Wang, Z.-L.; Wang, D. *Nano Lett.* **2009**, *9*, 2926−2934.
(27) Browning, N. D.; Chisholm, M. F.; Pennycook, S. J. *Nature* **1993**, *366*, 143−146.
(28) Pennycook, S. J.; Boatner, L. A. *Nature* **1988**, *336*, 565−567.
(29) James, E. M.; Browning, N. D. *Ultramicroscopy* **1999**, *78*, 125−139.
(30) McGibbon, A. J.; Pennycook, S. J.; Angelo, J. E. *Science* **1995**, *269*, 519−521.
(31) Hytch, M. J.; Snoeck, E.; Kilaas, R. *Ultramicroscopy* **1998**, *74*, 131−146.
(32) Conesa-Boj, S.; Boioli, F.; Russo-Averchi, E.; Dunand, S.; Heiss, M.; Rüffer, D.; Wyrsch, N.; Ballif, C.; Miglio, L.; Fontcuberta i Morral, A. *Nano Lett.* **2014**, *14*, 1859−1864.
(33) Hÿtch, M. J.; Putaux, J.-L.; Pénisson, J.-M. *Nature* **2003**, *423*, 270−273.
(34) Ertekin, E.; Greaney, P. A.; Chrzan, D. C.; Sands, T. D. *J. Appl. Phys.* **2005**, *97*, 114325.
(35) Kästner, G.; Gösele, U. *Philos. Mag.* **2004**, *84*, 3803−3824.
(36) Glas, F. *Phys. Rev. B* **2006**, *74*, 121302(R).
(37) Jeppsson, M.; Dick, K. A.; Wagner, J. B.; Caroff, P.; Deppert, K.; Samuelson, L.; Wernersson, L.-E. *J. Cryst. Growth* **2008**, *310*, 4115−4121.
(38) Caroff, P.; Messing, M. E.; Borg, B. M.; Dick, K. A.; Deppert, K.; Wernersson, L.-E. *Nanotechnology* **2009**, *20*, 495606.
(39) Guo, Y. N.; Zou, J.; Paladugu, M.; Wang, H.; Gao, Q.; Tan, H. H.; Jagadish, C. *Appl. Phys. Lett.* **2006**, *89*, 231917.
(40) Ercolani, D.; Rossi, F.; Li, A.; Roddaro, S.; Grillo, V.; Salviati, G.; Beltram, F.; Sorba, L. *Nanotechnology* **2009**, *20*, 505605.
(41) Caroff, P.; Wagner, J. B.; Dick, K. A.; Nilsson, H. A.; Jeppsson, M.; Deppert, K.; Samuelson, L.; Wallenberg, L. R.; Wernersson, L.-E. *Small* **2008**, *4*, 878−882.
(42) Jeppsson, M.; Dick, K. A.; Nilsson, H. A.; Sköld, N.; Wagner, J. B.; Caroff, P.; Wernersson, L.-E. *J. Cryst. Growth* **2008**, *310*, 5119−5122.
(43) Ek, M.; Borg, B. M.; Johansson, J.; Dick, K. A. *ACS Nano* **2013**, *7*, 3668−3675.
(44) Furtmayr, F.; Teubert, J.; Becker, P.; Conesa-Boj, S.; Morante, J. R.; Chernikov, A.; Schäfer, S.; Chatterjee, S.; Arbiol, J.; Eickhoff, M. *Phys. Rev. B* **2011**, *84*, 205303.
(45) Kanungo, P. D.; Schmid, H.; Björk, M. T.; Gignac, L. M.; Breslin, C.; Bruley, J.; Bessire, C. D.; Riel, H. *Nanotechnology* **2013**, *24*, 225304.
(46) Popovitz-Biro, R.; Kretinin, A.; Von Huth, P.; Shtrikman, H. *Cryst. Growth Des.* **2011**, *11*, 3858−3865.
(47) Arbiol, J.; Magen, C.; Becker, P.; Jacopin, G.; Chernikov, A.; Schäfer, S.; Furtmayr, F.; Tchernycheva, M.; Rigutti, L.; Teubert, J.; Chatterjee, S.; Morante, J. R.; Eickhoff, M. *Nanoscale* **2012**, *4*, 7517−7524.
(48) Xu, T.; Dick, K. A.; Plissard, S.; Nguyen, T. H.; Makoudi, Y.; Berthe, M.; Nys, J.-P.; Wallart, X.; Grandidier, B.; Caroff, P. *Nanotechnology* **2012**, *23*, 095702.
(49) Fontcuberta i Morral, A.; Arbiol, J.; Prades, J. D.; Cirera, A.; Morante, J. R. *Adv. Mater.* **2007**, *19*, 1347−1351.
(50) Bernal, S.; Botana, F. J.; Calvino, J. J.; López-Cartes, C.; Pérez-Omil, J. A.; Rodríguez-Izquierdo, J. M. *Ultramicroscopy* **1998**, *72*, 135−164.
(51) Arbiol, J.; Cirera, A.; Peiró, F.; Cornet, A.; Morante, J. R.; Delgado, J. J.; Calvino, J. J. *Appl. Phys. Lett.* **2002**, *80*, 329−331.
(52) Grillo, V.; Rotunno, E. *Ultramicroscopy* **2013**, *125*, 97−111.
(53) Zamani, R. R.; Ibáñez, M.; Luysberg, M.; Garcia-Castello, N.; Houben, L.; Prades, J. D.; Grillo, V.; Dunin-Borkowski, R. E.; Morante, J. R.; Cabot, A.; Arbiol, J. *ACS Nano* **2014**, *8*, 2290−2301.
(54) Grillo, V. *Microsc. Microanal.* **2011**, *17*, 1292−1293.
(55) Lugani, L.; Ercolani, D.; Sorba, L.; Sibirev, N. V.; Timofeeva, M. A.; Dubrovskii, V. G. *Nanotechnology* **2012**, *23*, 095602.
(56) Lugani, L.; Ercolani, D.; Rossi, F.; Salviati, G.; Beltram, F.; Sorba, L. *Cryst. Growth Des.* **2010**, *10*, 4038−4042.
(57) Arbiol, J.; Fontcuberta i Morral, A.; Estradé, S.; Peiró, F.; Kalache, B.; Roca i Cabarrocas, P.; Morante, J. R. *J. Appl. Phys.* **2008**, *104*, 064312.
(58) Kavanagh, K. L. *Semicond. Sci. Technol.* **2010**, *25*, 024006.
(59) Erni, R.; Rossell, M. D.; Kisielowski, C.; Dahmen, U. *Phys. Rev. Lett.* **2009**, *102*, 096101.
(60) Kisielowski, C.; Freitag, B.; Bischoff, M.; van Lin, H.; Lazar, S.; Knippels, G.; Tiemeijer, P.; van der Stam, M.; von Harrach, S.; Stekelenburg, M.; Haider, M.; Uhlemann, S.; Müller, H.; Hartel, P.; Kabius, B.; Miller, D.; Petrov, I.; Olson, E. A.; Donchev, T.; Kenik, E. A.; Lupini, A. R.; Bentley, J.; Pennycook, S. J.; Anderson, I. M.; Minor, A. M.; Schmid, A. K.; Duden, T.; Radmilovic, V.; Ramasse, Q. M.; Watanabe, M.; Erni, R.; Stach, E. A.; Denes, P.; Dahmen, U. *Microsc. Microanal.* **2008**, *14*, 469−477.
(61) de la Mata, M.; Magen, C.; Gazquez, J.; Utama, M. I. B.; Heiss, M.; Lopatin, S.; Furtmayr, F.; Fernández-Rojas, C. J.; Peng, B.; Morante, J. R.; Rurali, R.; Eickhoff, M.; Fontcuberta i Morral, A.; Xiong, Q.; Arbiol, J. *Nano Lett.* **2012**, *12*, 2579−2586.
(62) Uccelli, E.; Arbiol, J.; Magen, C.; Krogstrup, P.; Russo-Averchi, E.; Heiss, M.; Mugny, G.; Morier-Genoud, F.; Nygård, J.; Morante, J. R.; Fontcuberta i Morral, A. *Nano Lett.* **2011**, *11*, 3827−3832.
(63) Utama, M. I. B.; Belarre, F. J.; Magen, C.; Peng, B.; Arbiol, J.; Xiong, Q. *Nano Lett.* **2012**, *12*, 2146−2152.
(64) Utama, M. I. B.; de la Mata, M.; Magen, C.; Arbiol, J.; Xiong, Q. *Adv. Funct. Mater.* **2013**, *23*, 1636−1646.
(65) Dheeraj, D. L.; Patriarche, G.; Zhou, H.; Hoang, T. B.; Moses, A. F.; Grønsberg, S.; van Helvoort, A. T.; Fimland, B. O.; Weman, H. *Nano Lett.* **2008**, *8*, 4459−4463.
(66) Borg, B. M.; Dick, K. A.; Eymery, J.; Wernersson, L.-E. *Appl. Phys. Lett.* **2011**, *98*, 113104.
(67) Wang, J.; Plissard, S. R.; Verheijen, M. A.; Feiner, L.-F.; Cavalli, A.; Bakkers, E. P. A. M. *Nano Lett.* **2013**, *13*, 3802−3806.
(68) Svensson, S. F.; Jeppesen, S.; Thelander, C.; Samuelson, L.; Linke, H.; Dick, K. A. *Nanotechnology* **2013**, *24*, 345601.
(69) Oh, S. H.; Chisholm, M. F.; Kauffmann, Y.; Kaplan, W. D.; Luo, W.; Rühle, M.; Scheu, C. *Science* **2010**, *330*, 489−493.
(70) Wen, C.-Y.; Tersoff, J.; Hillerich, K.; Reuter, M. C.; Park, J. H.; Kodambaka, S.; Stach, E. A.; Ross, F. M. *Phys. Rev. B* **2011**, *107*, 025503.
(71) Wang, H.; Zepeda-Ruiz, L. A.; Gilmer, G. H.; Upmanyu, M. *Nat. Commun.* **2013**, *4*, 1956.
(72) Falub, C. V.; von Känel, H.; Isa, F.; Bergamaschini, R.; Marzegalli, A.; Chrastina, D.; Isella, G.; Müller, E.; Niedermann, P.; Miglio, L. *Science* **2012**, *335*, 1330−1334.
(73) Rocher, A. M. *Solid State Phenom.* **1991**, *19/20*, 563−572.
(74) Huang, S. H.; Balakrishnan, G.; Khoshakhlagh, A.; Jallipalli, A.; Dawson, L. R.; Huffaker, D. L. *Appl. Phys. Lett.* **2006**, *88*, 131911.